Electrochimica Acta 449 (2023) 142196

Contents lists available at ScienceDirect

Electrochimica Acta

journal homepage: www.journals.elsevier.com/electrochimica-acta

Welding and galvanic coupling effects on the electrochemical activity of dissimilar AA2050 and AA7050 aluminum alloys welded by Friction Stir Welding (FSW)

Bárbara Victoria G. de Viveiros *, Rejane Maria P. da Silva *, Uyime Donatus, Isolda Costa *

Instituto de Pesquisas Energéticas e Nucleares, IPEN/CNEN, Av. Prof. Lineu Prestes, 2242, São Paulo, Brazil

ARTICLE INFO

Keywords:
Dissimilar aluminum alloys
Friction stir welding
Galvanic coupling
Local electrochemical activity
SVET
Micropotentiometry

ABSTRACT

In this work, the effects of friction stir welding (FSW) on the microstructure and electrochemical activities of dissimilar AA2050 and AA7050 aluminum alloys have been investigated. Local electrochemical tests supported by surface analytical characterization were used to study the local electrochemical activities developed along the weld zones of the dissimilar alloys. The investigation was carried out on the cross-section of the welded Al alloys. The results showed that the friction stir welding (FSW) of the dissimilar alloys affected the microstructure and the electrochemical behavior of the different regions (HAZ, TMAZ, SZ) formed by the welding process. Scanning vibrating electrode technique (SVET) and micropotentiometry by using an ion-selective microelectrode showed that TMAZ was the zone with the highest electrochemical activity. This zone corresponded to the transition region between the two welded alloys. The high electrochemical activity observed in this region was associated with the effect of welding on the microstructure and, also, with the galvanic coupling between the two alloys, where the alloy AA7050 acted as an anode and the AA2050 as a cathode. Preferential corrosion attack on the AA7050 alloy was also evident.

1. Introduction

The Al alloys most commonly employed in the aeronautic industry are those from the 2XXX and 7XXX series [1–3]. These alloys have good mechanical properties due to precipitation hardening (resulting from their alloying elements), and low density [4]. However, they are susceptible to localized corrosion and when welded, their microstructures undergo changes that alter their properties [1,4]. Due to their poor weldability, Al alloy parts used in aircraft are joined by rivets resulting in increased weight [4]. Friction stir welding (FSW) is an alternative process to the use of rivets in aircraft parts made of Al alloys [5–8].This process has various advantages over conventional welding ones [9,10], since, during FSW, the materials do not reach their melting point. Still, FSW affects the material microstructure, and, consequently, their corrosion resistance, due to plastic deformation and the high temperatures reached during the welding process [11–13]. Also, when dissimilar aluminum alloys are welded by FSW, besides the microstructural change, there is also the likelihood of galvanic coupling activities between the zones of different chemical composition and metallurgical characteristics [1] in contact with each other, decreasing their corrosion resistance. The FSW process exposes the alloys to thermomechanical effects, producing different zones in the two alloys. The zones in the welded alloys are known as the stir zone (SZ), heat affected zone (HAZ), thermomechanically affected zone (TMAZ) and the base metal (BM) that is not affected by the welding process [7,8,14].

Various works have reported the corrosion behaviors of the different zones formed by the FSW process [1,9,11,15–21]. In these works, the authors revealed that enhanced corrosion activity can occur due to the microstructural changes and, in the case of dissimilar alloys, galvanic coupling effects between the distinct zones produced by the FSW process. Wadeson et al. [17] reported that the edge regions of the TMAZ were preferentially corroded in the friction stir weld of the AA7108-T79 alloy. Proton et al. [9] showed that the HAZ of the 2050-T3 joint was the most susceptible to pitting corrosion. Bousquet et al. [21] reported that the HAZ domain close to the TMAZ region of an AA2024-T3 was more sensitive to corrosion activity.

Some works have described the corrosion activities of dissimilar Al alloys joined by the FSW process [1–3,22–28]. Some examples of dissimilar Al alloys of the 2XXX and 7XXX series are reported in [1–3, 25–28]. For instance, Bertoncello et al. [25] investigated the corrosion

* Corresponding authors at: Instituto de Pesquisas Energéticas e Nucleares, IPEN/CNEN - Av. Prof. Lineu Prestes, 2242, São Paulo, Brazil.
E-mail addresses: barbaravictoriaviveiros@gmail.com (B.V.G. de Viveiros), rejanep2silva@gmail.com (R.M.P. da Silva), icosta@ipen.br (I. Costa).

https://doi.org/10.1016/j.electacta.2023.142196
Received 16 December 2022; Received in revised form 4 March 2023; Accepted 5 March 2023
Available online 7 March 2023

Table 1
Chemical composition (wt.%) of the AA2050-T84 and AA7050-T7451.

Alloys	Cu	Li	Mg	Si	Mn	Fe	Zn	Zr	Al
AA2050-T84	3.46	0.88	0.30	0.02	0.30	0.04	0.01	0.09	Balance
AA7050-T7451	2.15	–	1.53	0.08	–	0.04	6.80	0.14	Balance

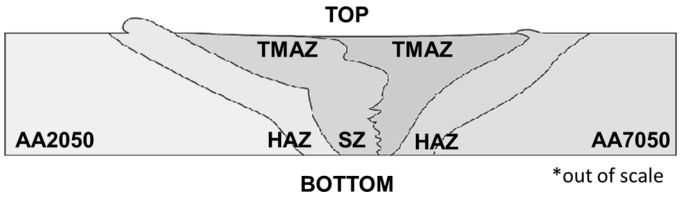

Fig. 1. Schematic drawing showing the weld zones from a cross section of the alloys AA2050 and AA7050 welded by FSW.

activity of friction stir lap weld of dissimilar AA7050 and AA2024 alloys by scanning vibrating electrode technique (SVET). In their work, the authors revealed galvanic coupling effects in the joint of the two materials. Sidane et al. [26] used the scanning electrochemical microscope (SECM) and local electrochemical impedance spectroscopy (LEIS) techniques to study the local electrochemical reactivity of weld zone interfaces in dissimilar friction stir weldment of AA2050-T8 and AA7449-T79 alloys. Using these local electrochemical techniques, the authors observed galvanic interactions between the 2050-T8 and the 7449-T749 Al alloys. De Abreu et al. [27] and Bugarin et al. [28] also reported galvanic coupling effects in the study of dissimilar AA2024/AA7475 alloys welded by FSW using LEIS technique [27] and by exposure of small areas to the corrosive environment [28].

Scanning probe electrochemical techniques were also successfully employed in the study of various Al alloys welded by FSW [29–33]. According to the authors, these techniques are useful in investigating the local electrochemical behavior of the different regions resulting from FSW processes.

In the present work, the localized corrosion resistance of the cross-section of dissimilar friction stir welded AA2050-T84 and AA7050-T7451 alloys was investigated. The local corrosion activity was studied by SVET and micropotentiometry by using an ion-selective microelectrode, which provides local electrochemical information about the activities of specific ions (such as H^+, Na^+, Cl^-, Mg^{2+}, etc.) in aqueous solutions, close to a reactive surface [34–36]. The use of SVET in combination with the micropotentiometry to investigate different zones of dissimilar Al alloys welded by FSW has not been carried out until now. In this study, tests using these scanning probe techniques were carried out in NaCl solution. The combination of the SVET and pH micropotentiometry enabled the precise identification of localized electrochemical activities and the nature of these activities across the weld zones of the dissimilar weld. The aim was to study the local electrochemical behavior above the distinct FSW zones, as well as the electrochemical interactions between them due to galvanic coupling.

2. Experimental

2.1. Materials

Samples of the AA2050-T84 and AA7050-T7451 aluminum alloys, whose chemical compositions are presented in Table 1, were used in this study.

Samples of the AA2050-T84 and AA7050-T7451 welded by FSW were sequentially ground with SiC papers of #400, #800, #1200, #2000, #2500, #4000 grit sizes and then polished with diamond pastes of 3 μm and 1 μm. After polishing, the samples were ultrasonically cleaned with ethanol, rinsed with deionized water and dried under a cold air stream.

2.2. Microstructural characterization, surface examination and corrosion test

The surfaces of the AA2050-T84 and AA7050-T7451 welded samples were examined by Optical Microscopy using a Leica DMLM coupled optical microscope (MO) and a HITACHI TM3000 scanning electron microscope (SEM), equipped with energy dispersive (EDS) detector and operated at 15 kV

The welded samples were chemically attacked in Weck's reagent, composed of 4 g $KMnO_4$, 0.1 L H_2O and 1 g NaOH, at room temperature. The samples were immersed in this solution for 15 s, rinsed with deionized water and then dried under a cold air stream.

Vickers microhardness measurements were performed using a Bueller 5112 microhardness tester, with a load of 300 gf and an indentation time of 15 s. Seven measurements were performed at each region, and the highest and smallest measurements were discarded. The mean and standard deviation of the measurements were then estimated for each region of the weld.

Immersion tests were carried out in a 3.5 wt.% NaCl solution for 3 days using only a reduced area (0.5 × 0.5 cm) of the TMAZ and SZ. The 3.5 wt.% NaCl solution was chosen to simulate sea-water conditions. After immersion tests, the exposed surface was analyzed by optical profilometry using the ZYGO's ZeGage™ equipment to investigate the average depth of corrosion penetration at the attacked regions.

2.3. Electrochemical characterization

Electrochemical characterization was carried out in a naturally aerated 5 × 10^{-3} mol L^{-1} NaCl solution at room temperature, Open circuit potential (OCP) measurements were initially obtained for 7 h. The less aggressive NaCl solution was chosen for the electrochemical characterization to make it easier to follow the evolution of the electrochemical activities. Local electrochemical tests were performed by scanning vibrating electrode technique (SVET), using an *Applicable Electronics™ SVET equipment*, which is controlled by *Automated Scanning Electrode Technique ASET 4.0 (Science Wares™)*. The vibrating electrode used was an insulated Pt-Ir electrode. A 15 μm diameter platinum sphere was electrodeposited at its tip before starting SVET measurements. Calibration of the test equipment was carried out using a 60 nA current with the calibration electrode, which was positioned 150 μm from the vibrating electrode. The conductivity of the solution was inputted in the *ASET 4 software*. Based on the inputted value, the potential difference was measured and automatically converted to current density values. For the SVET tests, the electrode vibrating in the perpendicular (Z) and parallel (X) planes to the sample surface was located at (100 ± 9) μm above the sample surface. The amplitude of vibration was 19 μm, and the vibration frequencies of the electrode were 174 Hz (X) and 73 Hz (Z). On each SVET map, 25×25 points were obtained. The time difference between a current density measurement and another was 0.52 s, and the scanning interval was 100 μm. All tests were performed in a Faraday cage at (20 ± 1) °C. The welded aluminum alloys, AA2050-T84 and AA7050-T7451, were used as working electrodes and the exposed surface area was 75 mm^2. The surfaces of the samples were polished to a 1 μm finish. Epoxy resin and adhesive tape were used to form the reservoir. The experiments were carried out in 5 × 10^{-3} mol L^{-1} NaCl solution for 24 h. SVET maps were obtained every 2 h, and in situ images of the exposed surface were obtained in this time intervals. An external

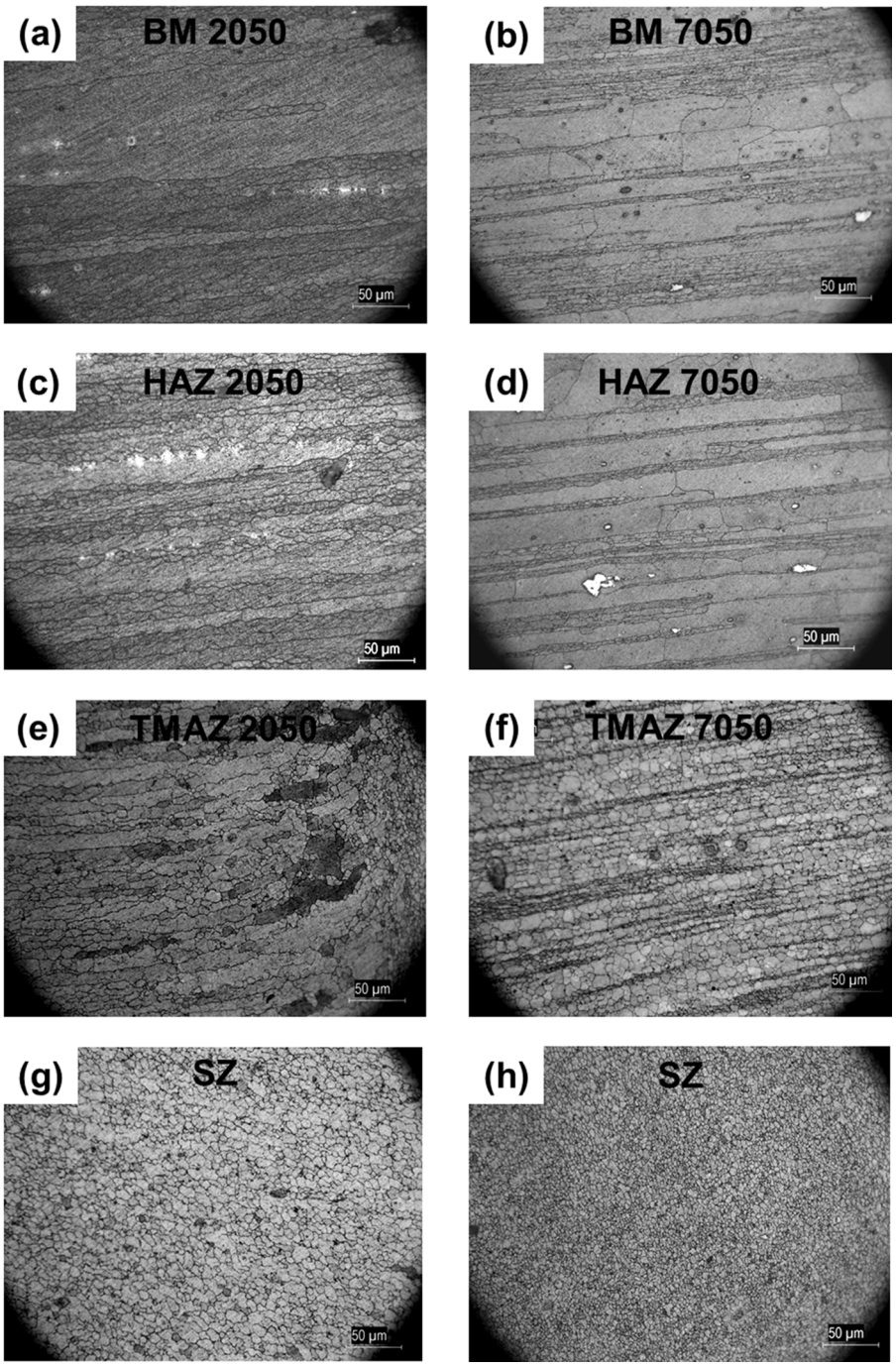

Fig. 2. Optical micrographs of the AA2050 and AA7050 surfaces welded by FSW. (a) AA2050 (BM). (b) AA7050 (BM). (c) AA2050 (HAZ). (d) AA7050 (HAZ). (e) AA2050 (TMAZ). (f) AA7050 (TMAZ). (g) upper areas of the SZ. (h) lower areas of the SZ.

reservoir was used with a 0.06 L electrolyte solution to maintain the same level of solution within the test vessel. A peristaltic pump was used to maintain the flow of the solution at a flow rate of 0.003 mL min^{-1}.

The local distribution of H^+ ions on the surfaces of the samples was acquired using micropotentiometry under open circuit conditions. The ion-selective microelectrode was made by back-filling silanized glass micropipetes with the inner filling solution (1×10^{-2} mol L^{-1} KH_2PO_4 in 0.1 mol L^{-1} KCl) and tip filling with hydrogen ionophore II cocktail A (Fluka). A chlorinated silver wire was inserted into the capillary resulting in the H^+ selective microelectrode. An Ag/AgCl electrode with KCl solution was used as an external reference electrode. The pH response of the pH- microelectrode was calibrated in a set of pH buffers. A linear relationship was observed between the solution pH and the potential response, with a slope of −45 mV per pH unit, in the 2 ≤pH ≤10 range (see Fig. S1). Although the slope of the calibration curve is less than the Nernstian slope, this is not unusual for pH- microelectrode [33]. The selective microelectrode was located at (50 ± 3) µm above the surface. All tests were performed in a Faraday cage at (20 ± 2) °C. The samples used as the working electrode were embedded in epoxy resin and their surfaces were sequentially polished. An adhesive tape and epoxy resin were used as a reservoir for the electrolyte (solution with 5 $\times 10^{-3}$ mol L^{-1} of NaCl, whose measured pH was 5.7) with a 2 h test duration.

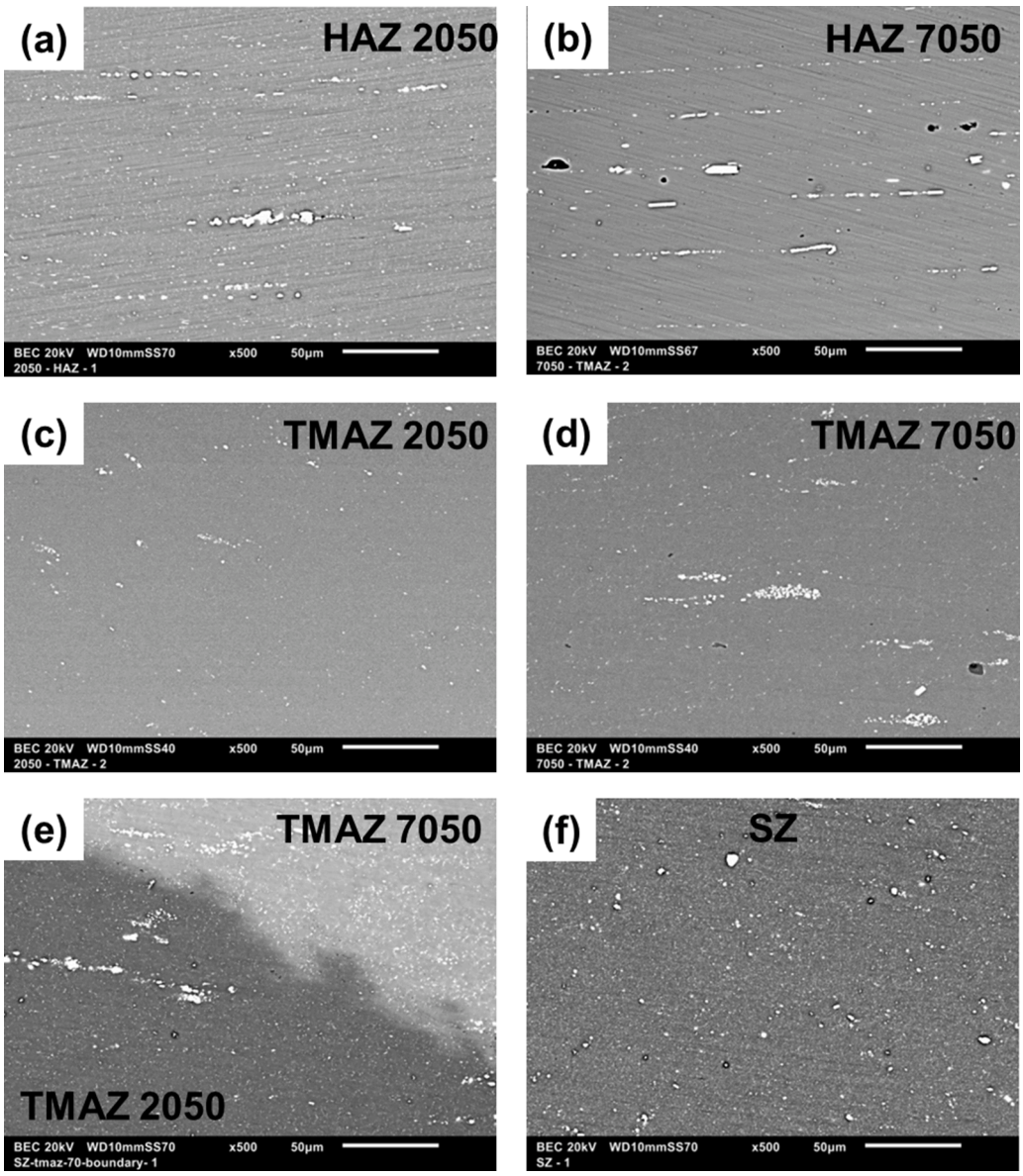

Fig. 3. SEM micrographs of the welded zones. (a) AA2050 (HAZ). (b) AA7050 (HAZ). (c) AA2050 (TMAZ). (d) AA7050 (TMAZ). (e) TMAZ transition zone between AA2050 and 7050. (f) SZ.

3. Results and discussion

3.1. Microstructural and surface characterization

The FSW affected and unaffected zones were studied after metallographic etching by analyzing the size and morphology of the grains. These zones were identified as the base metal (BM), heat affected zone (HAZ), thermomechanically affected zone (TMAZ) and stir zone (SZ). The different welding zones are shown schematically in Fig. 1 and microscopically in Fig. 2.

In the case of BMs, Fig. 2(a) and (b), there are larger grains in both alloys, where the welding process had no thermal or mechanical affect. In the case of the HAZs, Fig. 2 (c) and (d), the microstructure of these zones shows grain morphologies and grain sizes that are like those of the BMs. In the TMAZ, smaller grains are exhibited due to the high temperature and the mechanical effects of the stirring. Fig. 2 (e) and (F) show smaller grains than those in the HAZ due to the mechanical and heating process of the welding. Finally, the SZ, presents the smallest grains resulting from the recrystallization that has occurred due to the very high temperature and intense deformation (from the welding process) experienced in this zone, Fig. 2 (g) and (h). A difference can also be seen between the grain sizes at the top and bottom of the SZ.

The SEM images in Fig. 3 show the distribution of coarse second phase particles in the two welded alloys. Fig. 3(a) and (b) display the HAZ of the AA2050 and AA7050 alloys, respectively. In both cases, it is possible to identify the precipitates following the rolling direction. In the case of the HAZ of the AA7050 alloy, Fig. 3 (b), dark regions are observed. The dark regions corresponded to regions with highly reactive particles that were partially dissolved during polishing, and EDS analysis revealed high Mg peaks in these regions, Fig. 4. Analysis of the HAZ of the AA2050 alloy by EDS, Fig. 5, showed that the coarse particles were predominantly enriched in Fe and Cu.

The TMAZ of the two alloys, AA2050 and AA7050, shows that the particles are not agglomerated due to the mechanical tool movement during the welding process, leading to breakdown and drag of the particles which are redistributed at the near-surface, Fig. 3 (c) and (d). The transition zone between the TMAZ of the two alloys is easily identified due to the differences in chemical composition, Fig. 6. The AA7050 is

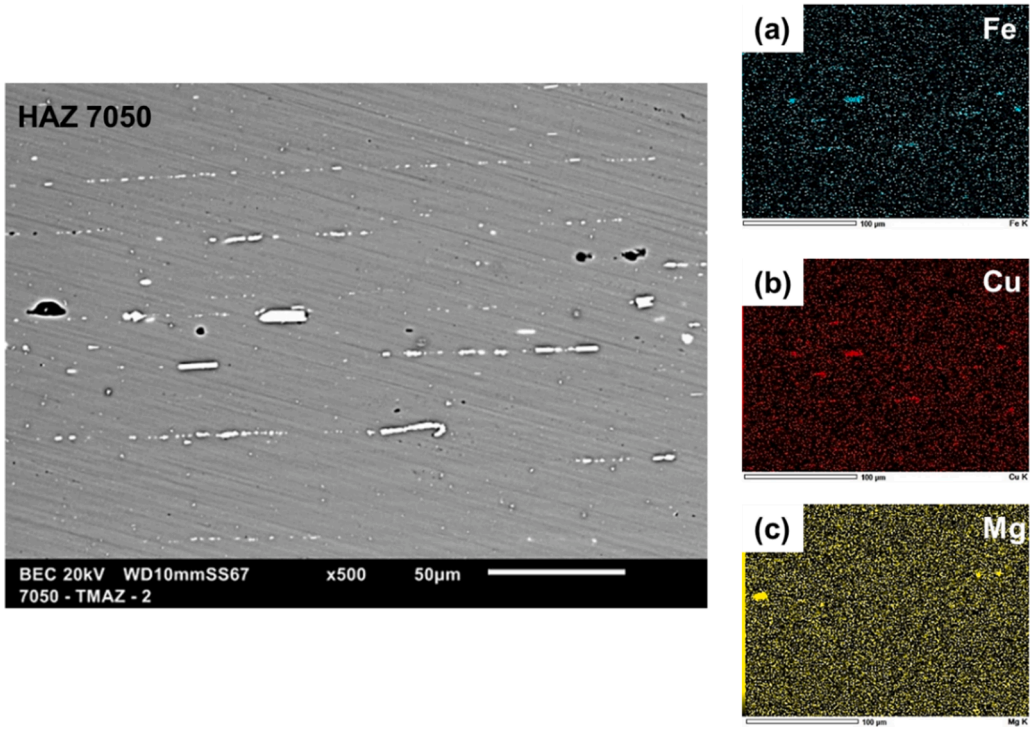

Fig. 4. SEM image and EDS maps of the HAZ of AA7050 showing the predominant elements in the second phase particles. (a) SEM image. (b) Fe EDS map. (c) Cu EDS map. (d) Mg EDS map.

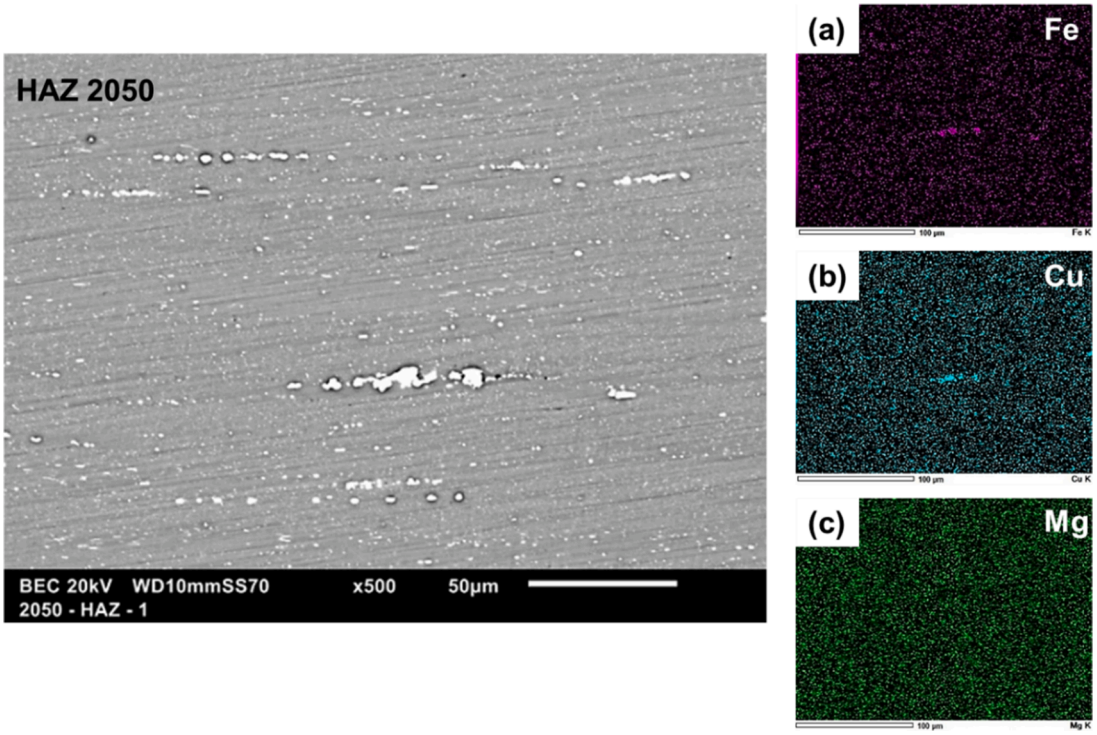

Fig. 5. SEM image and EDS maps of the HAZ of AA2050 showing the predominant elements in the second phase particles. (a) SEM image. (b) Fe EDS map. (c) Cu EDS map. (d). Mg EDS map.

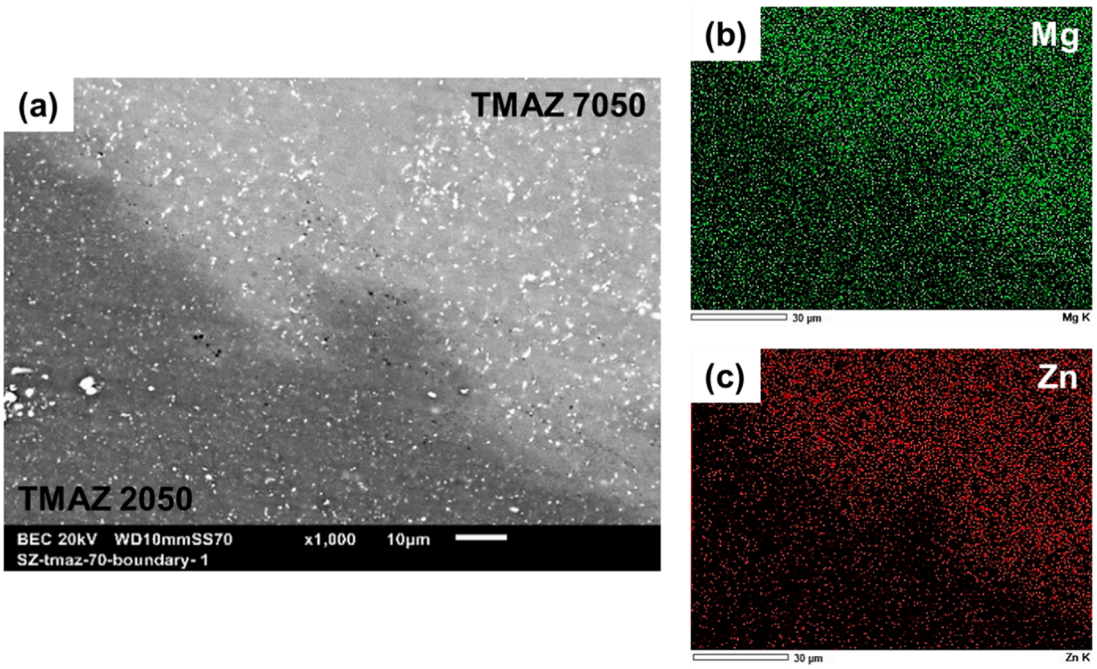

Fig. 6. SEM image and EDS maps of the TMAZ regions of the AA2050 and AA7050 alloys. (a) SEM image. (b) Mg EDS map. (c) Zn EDS map.

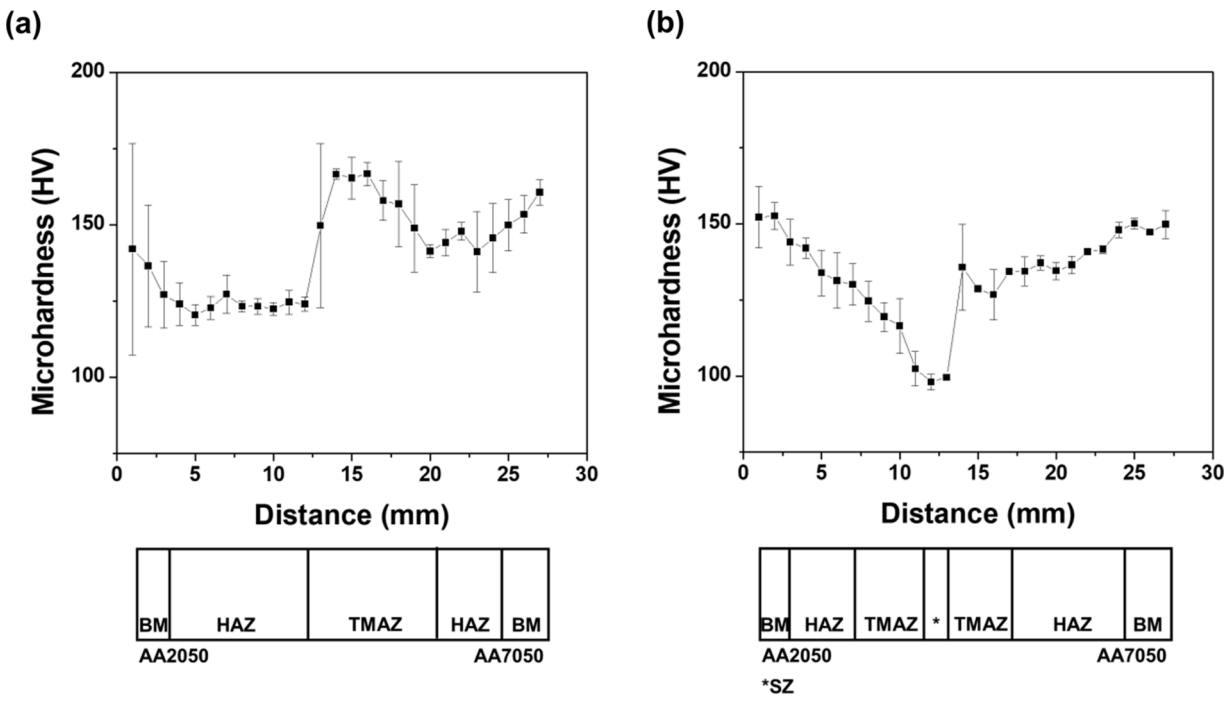

Fig.7. Microhardness plots obtained from (a) the near-surface region of the weldment and (b) bottom of the weldment.

richer in Mg and Zn than the AA2050. The SZ, Fig. 3 (F), shows a uniform and homogeneous distribution of particles over the entire surface when compared to the other regions affected by the welding.

Microhardness measurements across the weldment showed that the values varied across the different zones of the two alloys. This is explained by the changes in microstructure resulting from the heating and/or mechanical treatments, as shown in Fig. 7. The microhardness at the near-surface and the bottom zones of the HAZ of the AA2050 were compared. Lower microhardness values, between 110 HV and 120 HV, were recorded at the near-surface zone, Fig. 7(a). The microhardness values of the HAZ in the AA7050 were between 130 HV and 135 HV. From the results, it was difficult to establish the exact transition boundary between the HAZ and BM. As expected, the HAZ regions were wider at the near-surface compared with the bottom. This made it easier to obtain more BM value ranges (around 150 HV for both alloys) on the bottom side compared with the near-surface for the weldment width employed for the measurement. The highest microhardness values, among the tested zones, were associated with the AA2050-TMAZ, with values as high as 170 HV. The high microhardness values related to the TMAZ transition between AA2050 and AA7050 are explained by

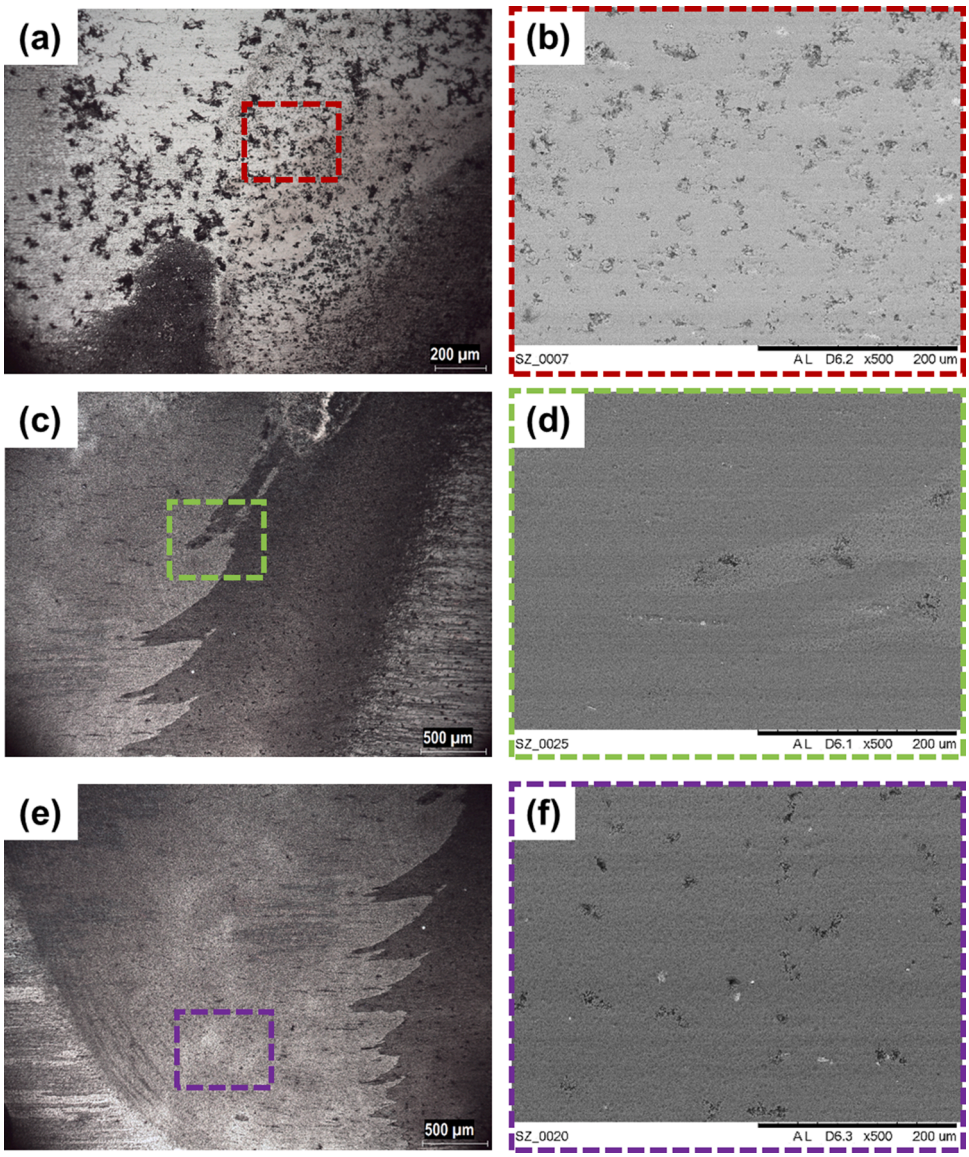

Fig. 8. Post-corrosion immersion test images of the SZ and transition zone in the TMAZ. (a) Optical image of the TMAZ of AA7050. (b) SEM image of the demarcated region in (a). (c) Optical image of the transition region between SZ and TMAZ of AA7050. (d) SEM image of the demarcated region in (c). (e) Optical image of the TMAZ of AA2050, SZ and TMAZ of AA7050. (f) SEM image of the SZ region demarcated in (e).

precipitation of particles during heating, as well as the plastic deformation of the grains, during the welding process. The decrease in hardness observed in the HAZ of the two alloys, on the other hand, indicates dissolution of hardening phases in both alloys due to thermal effects in this zone.

The lowest microhardness values were related to the bottom profile of the SZ, Fig. 7 (b), around 100 HV. In this zone, both recrystallization and dissolution of strengthening precipitates would have occurred and, therefore, a decrease in hardness is not unexpected. Jariyaboon et al. [1] also found similar microhardness results when the AA2024-T351 and AA7010-T7651 welded by FSW was analyzed and observed that the lowest hardness was related to the SZ. The results also show that the microhardness in the AA2050 alloy decreased from the BM to SZ, while for the AA7050 alloy, a decrease in hardness was not evident, with only slight variation in hardness between the BM and TMAZ, but a sharp decrease occurred between the TMAZ and SZ. These results suggest that the microstructure of the AA2050 alloy is more prone to variations due to heating and/or thermomechanical effects caused by FSW than the AA7050 alloy, for the welding conditions employed in this study.

Immersion tests carried out by exposing only a reduced area of the TMAZ and SZ to 3.5 wt.% NaCl solution, as indicated in Fig. 8, showed that the highest electrochemical activity was related to the TMAZ and SZ of the two alloys. The results showed that when galvanic coupling occurs, the AA7050-TMAZ is the zone of highest activity, Fig. 8 (d). The corrosion attack in the SZ is more homogeneously distributed, Fig. 8 (F). The region closest to the AA7050-TMAZ becomes cathodically protected, as evident when Fig. 8 (d) and (F) are compared. However, it must be mentioned that the TMAZ of the AA7050 alloy, which is further away from the galvanically coupled zones also presented corrosion attack, as shown in Fig. 8(a) and (b).

Fig. 9 presents the optical profilometry analyses of the surfaces of the welded alloys after 3 days of exposure to the 3.5 wt.% NaCl solution and after the removal of the corrosion products. The depth of attack penetration in the regions of intense localized attacks, specifically the SZ, AA7050-TMAZ and the transition region between the AA7050-TMAZ and SZ, Fig. 9. The region with the of lowest attack depth was the SZ. The transition region between the SZ and AA7050-TMAZ showed that the deepest penetration of attack occurred in the TMAZ of the AA7050

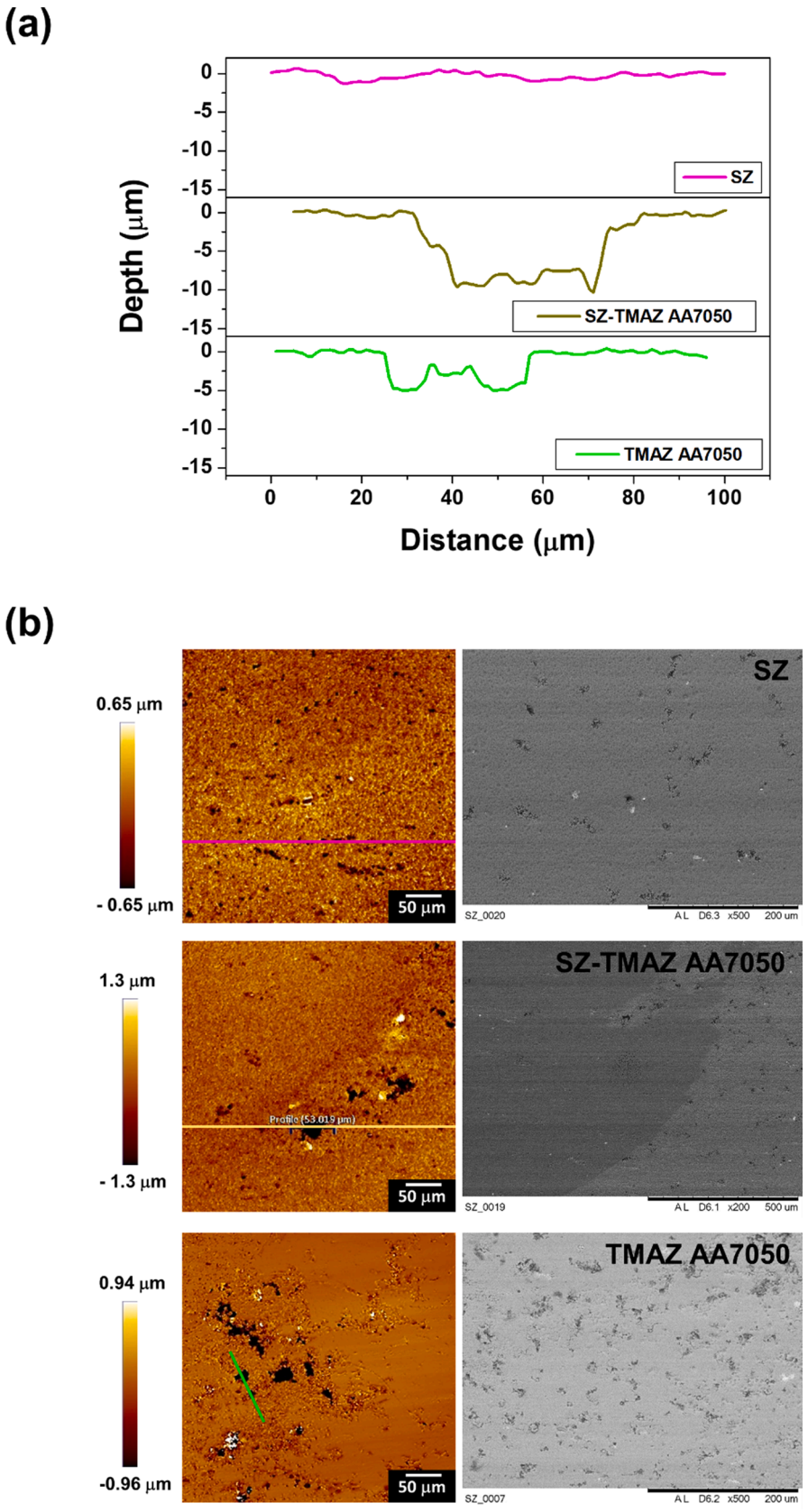

Fig. 9. Optical profilometry of the areas of highest corrosion activities on the AA2050 and AA7050 alloys welded by FSW. (a) Line scans of the SZ, SZ-TMAZ transition region of the AA7050 and TMAZ of the AA7050. (b) Optical images of the corroded zones.

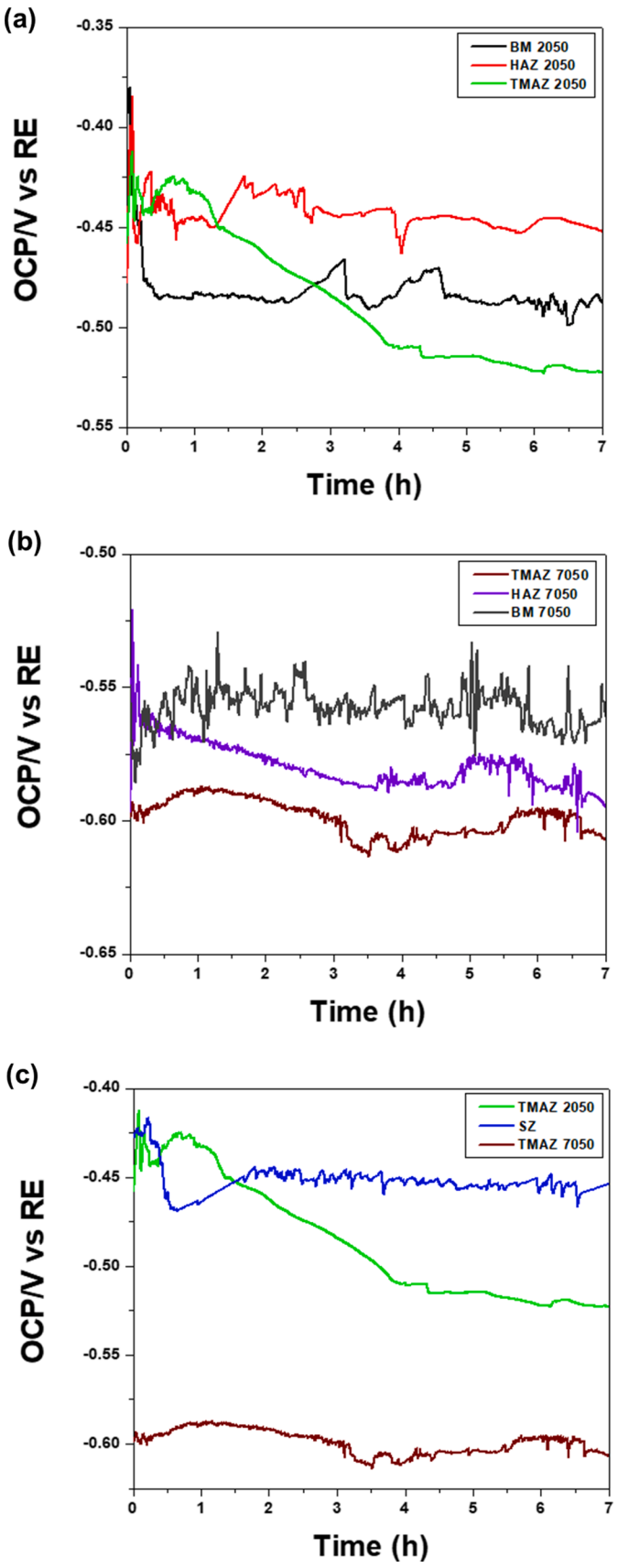

Fig. 10. OCP plots of the (a) AA2050 BM, HAZ and TMAZ, (b) AA7050 BM, HAZ and TMAZ, and (c) TMAZ zones of both alloys and the SZ.

alloy. Thus, the galvanic coupling between neighboring zones of different microstructures promoted corrosion penetration, and the zone that is most susceptible to localize attack is the AA7050-TMAZ coupled with the SZ.

The corrosion attack in the SZ was shallow and spread over a large area. The corrosion attack at the TMAZ of the AA7050, at areas far from the galvanic boundary, seems to be associated, mainly, with the precipitates at the grain boundaries leading to intergranular attack. Bertoncello et al. [25] also observed intergranular attack in both alloys, AA2024-T3 and AA7050-T76511, besides pitting, when these alloys were friction stir lap welded and exposed to 0.1 M NaCl. However, the intergranular attack penetration was deeper in the AA2024 compared to the AA7050 one.

3.2. Electrochemical characterization

3.2.1. Open circuit potential (OCP)

Open circuit potential measurements (Fig. 10) for each of the zones of both tested alloys were carried out in 5×10^{-3} mol L^{-1} NaCl solution for 7 h. The results showed that the TMAZ of the AA7050 is the most anodic region relative to the other zones. It was also possible to observe that the potential difference between the SZ and the TMAZ zones of the AA2050 alloy is approximately 50 mV, which is sufficient to drive galvanic activities between these zones.

3.2.2. Scanning vibrating electrode technique (SVET)

Fig. 11 shows SVET maps corresponding to 2 h and 24 h of test. These maps show that the predominant anodic areas were the transition zone between the SZ and TMAZ of the AA7050, as indicated by the OCP measurements, Fig. 10 (c), and immersion test, Fig. 8 (c) and (d). The cathodic areas were mainly the TMAZ of the AA2050 alloy and the SZ, and this was due to galvanic coupling effects. Bertoncello et al. [25] studied the alloys AA2024 and AA7050 welded by FSW using the SVET and observed that pits were mainly found on the AA7050 whereas the cathodic zones were mostly on the AA2024 region outside the SZ.

The highest anodic current densities, according to the SVET maps, decreased with time of test, possibly due to precipitation of corrosion products, and, after 24 h of test, the anodic region with high current densities reduced in size compared with that of the first hours of exposure (Fig. 11(a)-(b)).

Fig. 12 shows that the region mostly attacked by corrosion was the transition zone in the TMAZ. In this region, the anodic areas were located on the side of the AA7050 alloy, and the neighboring regions composed of the AA2050 alloy were cathodically protected. A more thorough observation of the anodic regions in the AA7050 alloy shows that attack propagation occurred via grain boundaries - intergranular corrosion was observed, as Fig. 12 shows, and this could be due to the presence of anodically active nanometric ($MgZn_2$) precipitates in the AA7050 alloy. On some of the attacked regions, deposited corrosion products were seen, confirming the hypothesis that this is one of the reasons for current reduction as indicated by the SVET results.

The regions indicated by numbers 1, 2 and 3 in Fig. 12(a) were related to the highest anodic current densities. The cathodically protected regions - the bright areas in Fig. 12 (b), (c) and (d) - occurred near the regions of highest anodic current densities. The transition regions of the TMAZ, between the AA2050 (TMAZ) alloy and the SZ, located at the interface with the AA7050 (TMAZ), are cathodically protected. These confirm that galvanic coupling has a significant effect on the electrochemical behavior of the welded alloys tested in this study.

SVET analysis of a reduced region of the weld was performed, specifically at the interfacial zone between the two alloys in this study. The interfacial zones correspond to the transition region in the TMAZ of the weld and the SZ/TMAZ interface. Galvanic coupling effect is expected based on the OCP results presented earlier, Fig. 10 (c). SVET maps obtained for this reduced area after 2 h, 12 h and 24 h of exposure to 5×10^{-3} mol L^{-1} NaCl solution are shown in Fig. 13.

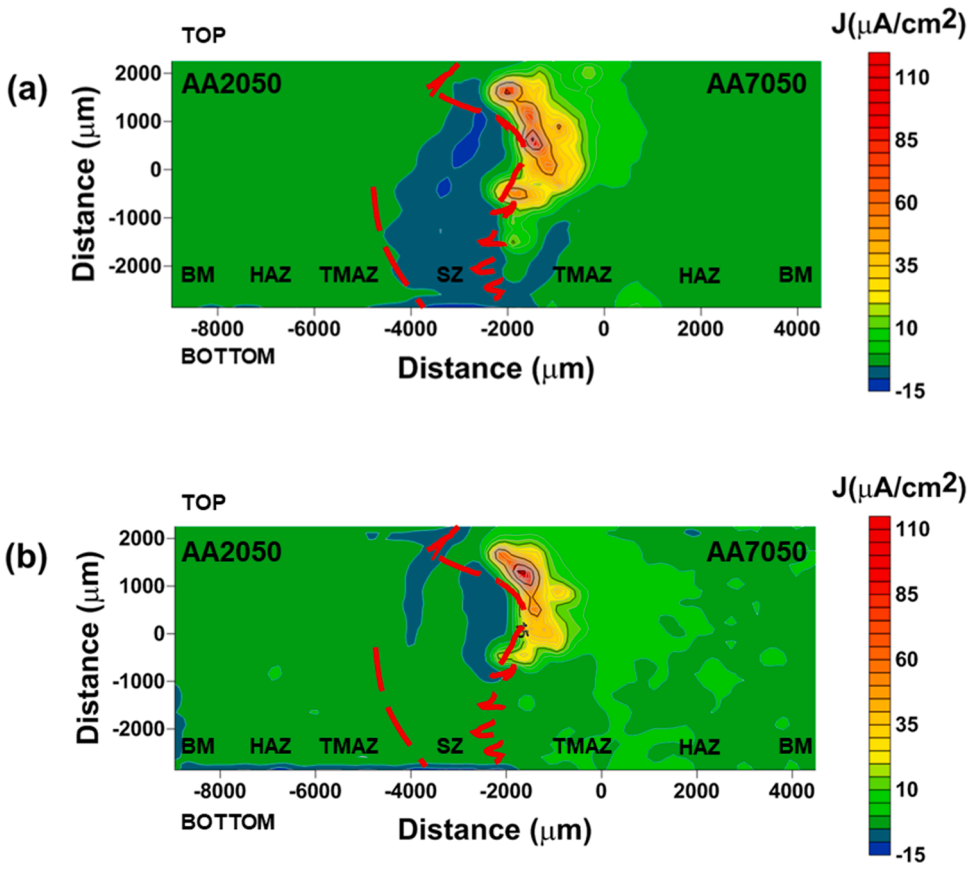

Fig. 11. SVET maps of AA2050 and AA7050 alloys welded by FSW after exposure to 5×10^{-3} mol L^{-1} of NaCl solution for (a) 2 h and (b) 24 h.

These maps clearly show that the interface between the alloys exhibits the highest electrochemical activity, with several anodic areas, all located in the AA7050 alloy side, while the cathodic ones are on the side of the AA2050 alloy. The anodic current densities in the first hours of test which were around 20 μA cm^{-2}, Fig. 13(a), increased with time and after 24 h, the values reached 100 μA cm^{-2}, showing that the corrosion process continues over the time of test. These results show the effect of galvanic coupling by indicating higher electrochemical activity at the interface between the two alloys. This is in accordance with the Fig. 11, which shows less electrochemical activities in the BM/HAZ away from the weld zone, particularly at the boundary between the two alloys.

The surface exposed to the test solution is shown in Fig. 14, before and after the removal of the corrosion products, after 24 h of exposure. Several points of intense corrosion attack were seen in the TMAZ of the AA7050 alloy, indicating the propagation of corrosion by intergranular attack. Bugarin et al. [28] investigated the electrochemical behavior of the AA2024-T3 alloy galvanically coupled to the AA7475-T651 alloy due to friction stir welding of both alloys and observed intergranular attack in the AA7475 alloy related to precipitates composed of Mg and Zn, which are the main constituents of the η phase, mainly located at the grain boundaries. It is likely that the intergranular attack observed in the AA7050 of this study is also due to the presence of grain boundary precipitates in the AA7050 alloy, which it can be seen in Viveiros et al. [37]. The micrographs show corrosion penetration via grain boundaries and deposited corrosion products on some pits that were revealed after the removal of the products, Fig. 14 (b), (d) and (F). The results confirmed galvanic coupling effects in the transitional TMAZ region and SZ where the two alloys and zones interface with one another.

3.2.3. *Micropotentiometry*

pH micropotentiometry results corresponding to 2 h of exposure to 5×10^{-3} mol L^{-1} NaCl solution are shown in Fig. 15. The blue color scale is associated with regions of higher pH, while the red scale is associated with the ones of lower pH. The local pH of the solution on the region most susceptible to corrosion reached values of around 3.5; while on the part of the AA2050 alloy and SZ, immediately adjacent to the AA7050 alloy, the pH values of the solution reached values of 7.1. This result shows a large pH difference at the transition zone between the welded alloys. The cathodic areas are related to the AA2050 alloy zones and the SZ, as expected.

In aerated alkaline or neutral pH electrolytes, the reduction of oxygen is the main cathodic process, as indicated by reaction (1). Thus, the oxygen reduction causes the localized alkalinization at the cathodic sites. Conversely, in the anodic regions, the major reaction is the metal dissolution, according to reaction (2), followed by hydrolysis stimulated by the metallic cations, which lead to pH decrease, as indicated in reaction (3). A second cathodic activity also occurs at the active dissolution front from within the pit (where the pH is so low) according to Eq. (4).

$$O_2 + 2H_2O + 4e^- \rightarrow 4OH^- \quad (1)$$

$$Al \rightarrow Al^{3+} + 3e^- \quad (2)$$

$$Al^{3+} + 3H_2O \rightarrow Al(OH)_3 + 3H^+ \quad (3)$$

$$2H^+ + 2e^- \rightarrow H_2 \quad (4)$$

The predominant anodic region in Fig. 15(a) corresponds to the

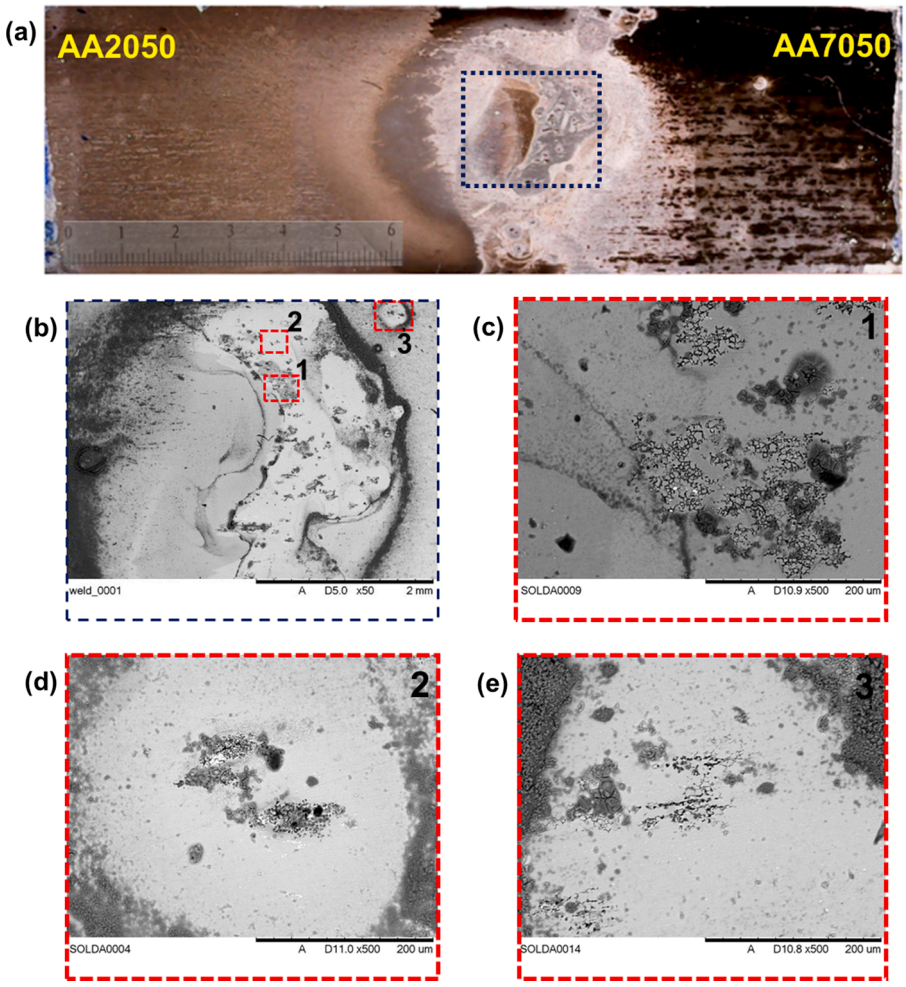

Fig. 12. (a) Optical image showing the whole exposed surface during SVET test. (b) SEM image of the Interface between SZ and TMAZ of the AA7050. (c) SEM image showing intergranular corrosion in the TMAZ of the AA7050, specifically in area 1 in (b). (d) SEM image showing intergranular corrosion in TMAZ 7050, specifically in area 2 in (b). (e) SEM image showing intergranular corrosion in TMAZ of the 7050, specifically in area 3 in (b).

AA7050-TMAZ. The low pH values are corroborated by the evolution of hydrogen bubbles in the most anodic active areas of this alloy, but also indicate that cathodic reactions (reduction of hydrogen ions with gas bubble formation according to reaction (4)) must occur inside the cavities due to corrosion in the AA7050 alloy, caused by corrosion penetration into the material. The corrosion activity at these regions is autocatalytic and favors the constant production of hydrogen bubbles. The results confirm that the AA7050-TMAZ region was the most susceptible to the development of autocatalytic corrosion sites, resulting in localized acidification and, consequently, generation of hydrogen bubbles. The optical micrograph in Fig. 15 (b) shows the anodic region with the presence of hydrogen bubbles (arrows point to H_2 bubbles).

Therefore, the microelectrochemical results associated with the microstructural features show that the AA7050-TMAZ is anodic in relation to the other regions in the welded alloys and, consequently, displayed higher electrochemical activity. Furthermore, it is possible to verify that the electrochemical activity in the AA7050 is higher than in the AA2050, and this last alloy acted cathodically relative to the AA7050. According to the micropotentiometry tests (Fig. 15), the corrosion protected areas are related to the AA2050 alloy. Thus, the intense corrosive attack observed in the AA7050 alloy occurs due to the combination of the modified microstructure due to FSW and effective galvanic coupling between the welded alloys.

4. Conclusions

The results showed that friction stir welding of the dissimilar alloys, AA2050 and AA7050, affected their microstructure and electrochemical activities - producing different zones with distinct microstructure and electrochemical responses. These zones were the BM, HAZ, TMAZ and SZ. The pH micropotentiometry and SVET combination enabled the understanding of the localized electrochemical activities and the nature of these activities in these zones. The local electrochemical results showed that the zone with the highest electrochemical activity was TMAZ, precisely at the transition between the two welded alloys. The high electrochemical activity in this region was due to the galvanic coupling between the two alloys. The AA7050 acted as the anode while the AA2050 acted as the cathode. In the zone of highest electrochemical activity, intense evolution of hydrogen bubbles was observed. Higher susceptibility to corrosive attack in the AA7050 alloy and predominance of cathodic reactions on the AA2050 alloy were observed when the coupled alloys were compared with the isolated ones, confirming the significant effect of the galvanic coupling between the two welded alloys.

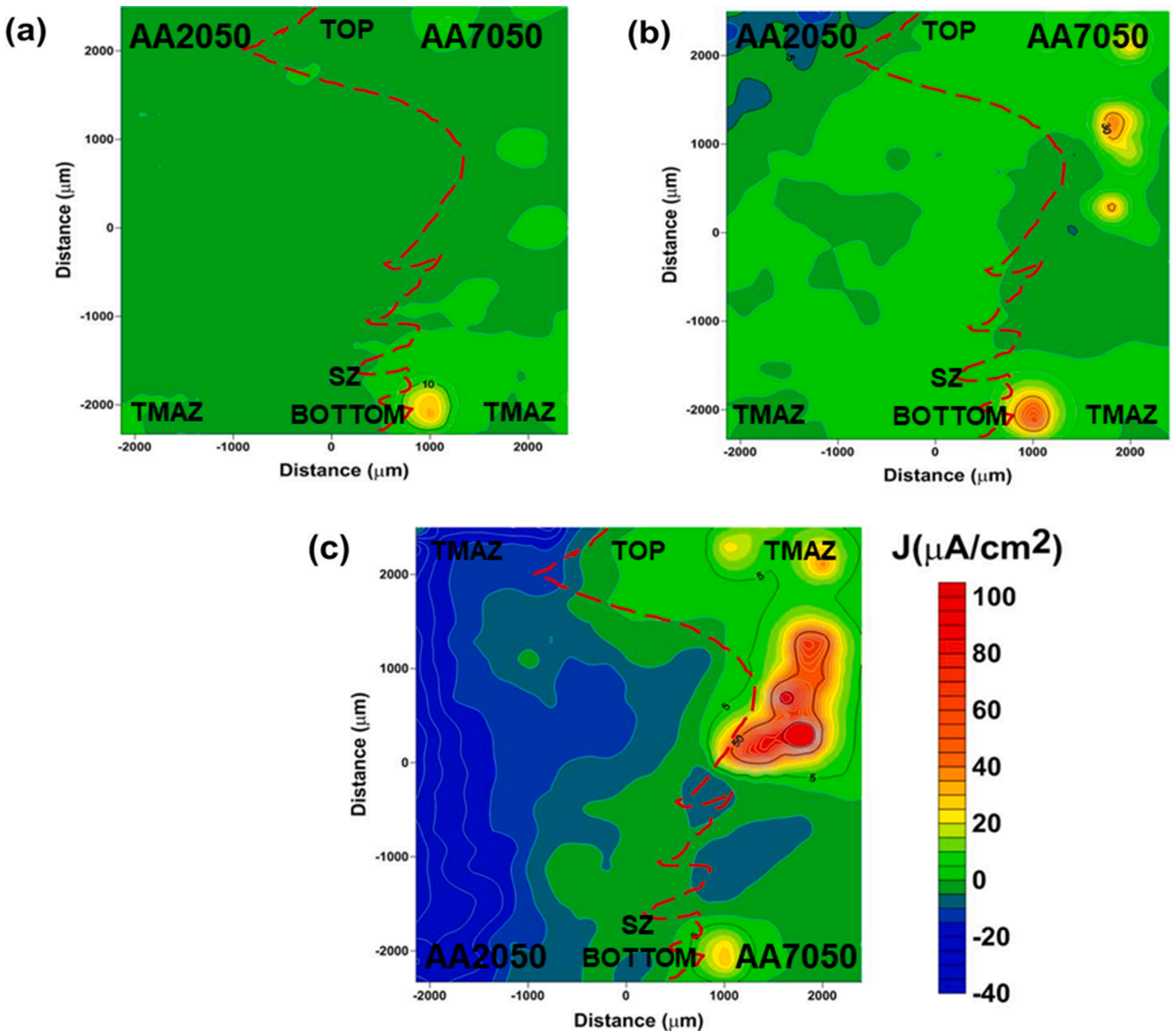

Fig. 13. SVET maps obtained using a reduced area of the AA2050 and AA7050 alloys welded by FSW after immersion in 5×10^{-3} mol L^{-1} of NaCl solution for (a) 2 h; (b) 12 h and (c) 24 h.

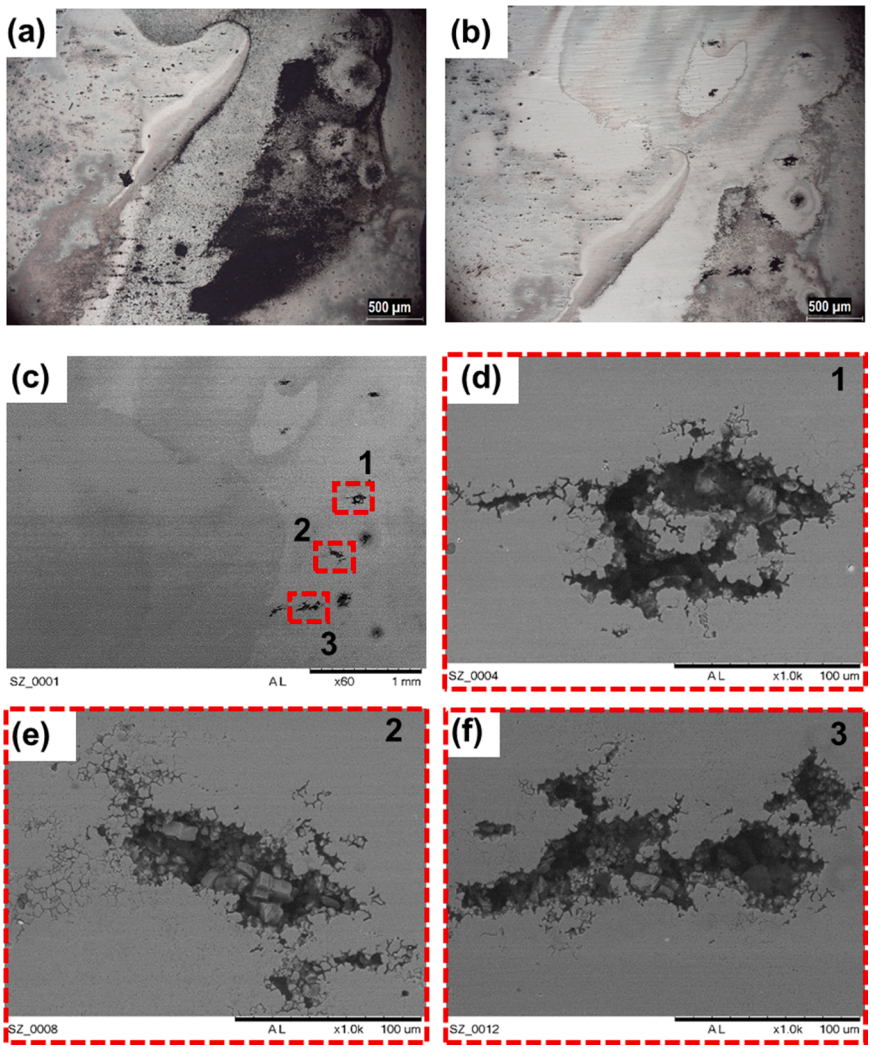

Fig. 14. Optical and SEM images showing corroded area after removal from the 5×10^{-3} mol L^{-1} of NaCl solution used in the SVET test. (a) Optical microscopy of the SZ and AA7050-TMAZ before desmutting. (b) Optical micrograph of SZ and AA7050-TMAZ after desmutting. (c) SEM image of SZ and AA7050-TMAZ after desmutting. (d) Magnified SEM image showing a pit at the AA7050-TMAZ, marked as 1 in (c). (e) Magnified SEM image of a pit at the AA7050-TMAZ marked as 2 in (c). (f) Magnified image of a pit at the AA7050-TMAZ marked as 3 in (c).

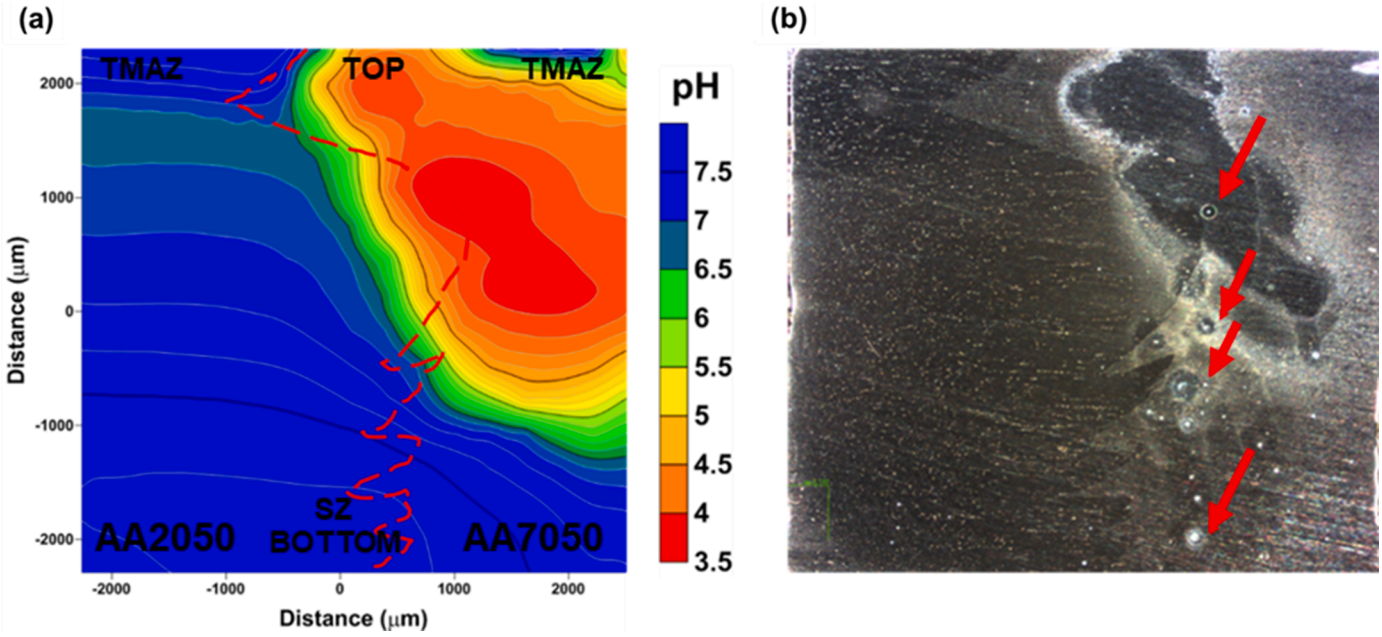

Fig. 15. Micropotentiometry maps obtained using a reduced area of the AA2050 and AA7050 alloys welded by FSW after (a) 2 h of immersion in 5×10^{-3} mol L^{-1} of NaCl solution; (b) Optical Micrograph of the sample after micropotentiometry test.

CRediT authorship contribution statement

Bárbara Victoria G. de Viveiros: Conceptualization, Investigation, Data curation, Validation, Visualization, Writing – original draft, Writing – review & editing. **Rejane Maria P. da Silva:** Conceptualization, Data curation, Validation, Visualization, Writing – original draft, Writing – review & editing. **Uyime Donatus:** Conceptualization, Data curation, Validation, Visualization, Writing – original draft, Writing – review & editing. **Isolda Costa:** Supervision, Resources, Funding acquisition, Writing – review & editing.

Declaration of Competing Interest

The authors declare that they have no known competing financial interests or personal relationships that could have appeared to influence the work reported in this paper.

Data availability

The raw/processed data required to reproduce these findings cannot be shared at this time as the data also forms part of an ongoing study.

Acknowledgments

The authors are thankful to CAPES (B.V.G. Viveiros) and FAPESP (Proc. 2013/13235-6, Proc. 2017/03095-3 and Proc. 2018/06880-6) for financial support for this work.

Supplementary materials

Supplementary material associated with this article can be found, in the online version, at doi:10.1016/j.electacta.2023.142196.

References

[1] M. Jariyaboon, A.J. Davenport, R. Ambat, B.J. Connolly, S.W. Williams, D.A. Price, Corrosion of a dissimilar friction stir weld joining aluminium alloys AA2024 and AA7010, Corrosion Engineering, Sci. Technol. 41 (2006) 135–142, https://doi.org/10.1179/174327806×107905.

[2] N.Z. Khan, A.N. Siddiquee, Z.A. Khan, A.K. Mukhopadhyay, Mechanical and microstructural behavior of friction stir welded similar and dissimilar sheets of AA2219 and AA7475 aluminium alloys, J. Alloys Compd. 695 (2017) 2902–2908, https://doi.org/10.1016/j.jallcom.2016.11.389.

[3] P.L. Niu, W.Y. Li, N. Li, Y.X. Xu, D.L. Chen, Exfoliation corrosion of friction stir welded dissimilar 2024-to-7075 aluminum alloys, Mater. Charact. 147 (2019) 93–100, https://doi.org/10.1016/j.matchar.2018.11.002.

[4] T. Dursun, C. Soutis, Recent developments in advanced aircraft aluminium alloys, Mater. Des. 56 (2014) 862–871, https://doi.org/10.1016/j.matdes.2013.12.002.

[5] P.F. Mendez, T.W. Eagar, Welding processes for aeronautics, Adv. Mater. Processes 159 (2001) 39–43.

[6] R.S. Mishra, Z.Y. Ma, Friction stir welding and processing, Mater. Sci. Eng. R: Rep. 50 (2005) 1–78, https://doi.org/10.1016/j.mser.2005.07.001.

[7] R. Nandan, T. Debroy, H.K.D.H. Bhadeshia, Recent advances in friction stir welding – process, Weldment structure and properties, Prog. Mater Sci. 53 (2008) 980–1023, https://doi.org/10.1016/j.pmatsci.2008.05.001.

[8] P.L. Threadgill, A.J. Leonard, H.R. Shercliff, P.J. Withers, Friction stir welding of aluminium alloys, Int. Mater. Rev. 54 (2009) 49–93, https://doi.org/10.1179/174328009×411136.

[9] V. Proton, J. Alexis, E. Andrieu, C. Blanc, J. Delfosse, L. Lacroix, Influence of post-welding heat treatment on the corrosion behavior of a 2050-t3 aluminum-copper-lithium alloy friction stir welding joint, J. Electrochem. Soc. 158 (2011) C139–C147, https://doi.org/10.1149/1.3562206.

[10] X. Zhang, B. Liu, X. Zhou, J. Wang, C. Luo, Z. Sun, Z. Tang, F. Lu, Corrosion behavior of friction stir welded 2A97 Al-Cu-Li alloy, Corrosion 73 (8) (2017) 988–997, 10.5006/2418.

[11] M. Jariyaboon, A.J. Davenport, R. Ambat, B.J. Connolly, S.W. Williams, D.A. Price, The effect of welding parameters on the corrosion behaviour of friction stir welded AA2024-T351, Corros. Sci. 49 (2007) 877–909, https://doi.org/10.1016/j.corsci.2006.05.038.

[12] J.C. Rao, E.J. Payton, C. Somsen, K. Neuking, G. Eggeler, A. Kostka, J.F. Dos Santos, Where does the lithium go? - A study of the precipitates in the stir zone of a friction stir weld in a Li-containing 2xxx series Al alloy, Adv. Eng. Mater. 12 (2010) 298–303, https://doi.org/10.1002/adem.200900284.

[13] W. Li, R. Jiang, Z. Zhang, Y. Ma, Effect of rotation speed to welding speed ratio on microstructure and mechanical behavior of friction stir welded aluminum–lithium alloy joints, Adv. Eng. Mater. 15 (2013) 1051–1058, https://doi.org/10.1002/adem.201300147.

[14] R.W. Fonda, J.F. Bingert, Precipitation and grain refinement in a 2195 Al friction stir weld, Metall. Mater. Trans. A 37 (2006) 3593–3604, https://doi.org/10.1007/s11661-006-1054-2.

[15] J.B. Lumsden, M.W. Mahoney, G. Pollock, C.G. Rhodes, Intergranular corrosion following friction stir welding of aluminum alloy 7075-T651, Corrosion 55 (1999) 1127–1135, https://doi.org/10.5006/1.3283950.

[16] J.B. Lumsden, M.W. Mahoney, C.G. Rhodes, G.A. Pollock, Corrosion behavior of friction-stir-welded AA7050-T7651, Corrosion 59 (2003) 212–219, https://doi.org/10.5006/1.3277553.

[17] D.A. Wadeson, X. Zhou, G.E. Thompson, P. Skeldon, L.D. Oosterkamp, G. Scamans, Corrosion behaviour of friction stir welded AA7108 T79 aluminium alloy, Corros. Sci. 48 (2006) 887–897, https://doi.org/10.1016/j.corsci.2005.02.020.

[18] C.S. Paglia, R.G. Buchheit, The time–temperature–corrosion susceptibility in a 7050-T7451 friction stir weld, Mater. Sci. Eng.: A 492 (2008) 250–254, https://doi.org/10.1016/j.msea.2008.03.039.

[19] J. Kang, R. Fu, G. Luan, C. Dong, M. He, In-situ investigation on the pitting corrosion behavior of friction stir welded joint of AA2024-T3 aluminium alloy, Corros. Sci. 52 (2010) 620–626, https://doi.org/10.1016/j.corsci.2009.10.027.

[20] P.B. Srinivasan, K.S. Arora, W. Dietzel, S. Pandey, M.K. Schaper, Characterisation of microstructure, mechanical properties and corrosion behaviour of an AA2219 friction stir weldment, J. Alloys Compd. 492 (2010) 631–637, https://doi.org/10.1016/j.jallcom.2009.11.198.

[21] E. Bousquet, A. Poulon-Quintin, M. Puiggali, O. Devos, M. Touzet, Relationship between microstructure, microhardness and corrosion sensitivity of an AA2024-T3 friction stir welded joint, Corros. Sci. 53 (2011) 3026–3034, https://doi.org/10.1016/j.corsci.2011.05.049.

[22] C. Shen, J. Zhang, J. Ge, Microstructures and electrochemical behaviors of the friction stir welding dissimilar weld, J. Environ. Sci. 23 (2011) S32–S35, https://doi.org/10.1016/S1001-0742(11)61072-3.

[23] H.S. Patil, S.N. Soman, Effect of weld parameter on mechanical and metallurgical properties of dissimilar joints AA6082–AA6061 in T6 condition produced by FSW, Frattura Ed Integrità Strutturale 7 (2013) 151–160, https://doi.org/10.3221/IGF-ESIS.24.16.

[24] U. Donatus, G.E. Thompson, X. Zhou, J. Wang, A. Cassell, K. Beamish, Corrosion susceptibility of dissimilar friction stir welds of AA5083 and AA6082 alloys, Mater. Charact. 107 (2015) 85–97, https://doi.org/10.1016/j.matchar.2015.07.002.

[25] J.C.B. Bertoncello, S.M. Manhabosco, L.F.P. Dick, Corrosion study of the friction stir lap joint of AA7050-T76511 on AA2024-T3 using the scanning vibrating electrode technique, Corros. Sci. 94 (2015) 359–367, https://doi.org/10.1016/j.corsci.2015.02.029.

[26] D. Sidane, E. Bousquet, O. Devos, M. Puiggali, M. Touzet, V. Vivier, A. Poulon-Quintin, Local electrochemical study of friction stir welded aluminum alloy assembly, J. Electroanal. Chem. 737 (2015) 206–211, https://doi.org/10.1016/j.jelechem.2014.06.025.

[27] C.P. de Abreu, I. Costa, H.G. de Melo, N. Pébère, B. Tribollet, V. Vivier, Multiscale electrochemical study of welded Al alloys joined by friction stir welding, J. Electrochem. Soc. 164 (2017) C735–C746, https://doi.org/10.1149/2.0391713jes.

[28] A.F.S. Bugarin, C.P. De Abreu, M. Terada, H.G. De Melo, I. Costa, Effect of friction stir welding (FSW) on the electrochemical behavior and galvanic coupling of AA2024-T3 and AA7475-T651, Materials Today Communications 25 (2020), 101591, https://doi.org/10.1016/j.mtcomm.2020.101591.

[29] U. Donatus, B.V.G. de Viveiros, M.C. de Alencar, R.O. Ferreira, M.X. Milagre, I. Costa, Correlation between corrosion resistance, anodic hydrogen evolution and microhardness in friction stir weldment of AA2198 alloy, Mater. Charact. 144 (2018) 99–112, https://doi.org/10.1016/j.matchar.2018.07.004.

[30] U. Donatus, R.M.P. da Silva, J.V. de Sousa Araujo, M.X. Milagre, C.P. de Abreu, C. de Souza Carvalho Machado, I. Costa, Macro and microgalvanic interactions in friction stir weldment of AA2198-T851 alloy, J. Mater. Res. Technol. 8 (2019) 6209–6222, https://doi.org/10.1016/j.jmrt.2019.10.015.

[31] F.M. Queiroz, U. Donatus, O.M. Prada Ramirez, J.V. de Sousa Araujo, B. V. Gonçalves de Viveiros, S. Lamaka, M. Zheludkevich, M. Masoumi, V. Vivier, I. Costa, H. Gomes de Melo, Effect of unequal levels of deformation and fragmentation on the electrochemical response of friction stir welded AA2024-T3 alloy, Electrochim. Acta 313 (2019) 271–281, https://doi.org/10.1016/j.electacta.2019.04.137.

[32] M.X. Milagre, U. Donatus, N.V. Mogili, R.M.P. Silva, B.V.G. de Viveiros, V. F. Pereira, R.A. Antunes, C.S.C. Machado, J.V.S. Araujo, I. Costa, Galvanic and asymmetry effects on the local electrochemical behavior of the 2098-T351 alloy welded by friction stir welding, J. Mater. Sci. Technol. 45 (2020) 162–175, https://doi.org/10.1016/j.jmst.2019.11.016.

[33] R.M.P. da Silva, J. Izquierdo, M.X. Milagre, A.M. Betancor-Abreu, L.A. de Oliveira, R.A. Antunes, R.M. Souto, I. Costa, On the local corrosion behavior of coupled welded zones of the 2098-T351 Al-Cu-Li alloy produced by Friction Stir Welding (FSW): an amperometric and potentiometric microelectrochemical investigation, Electrochim. Acta 373 (2021), 137910, https://doi.org/10.1016/j.electacta.2021.137910.

[34] S.V. Lamaka, O.V. Karavai, A.C. Bastos, M.L. Zheludkevich, M.G.S. Ferreira, Monitoring local spatial distribution of Mg2+, pH and ionic currents, Electrochem. Commun. 10 (2008) 259–262, https://doi.org/10.1016/j.elecom.2007.12.003.

[35] M. Taryba, S.V. Lamaka, D. Snihirova, M.G.S. Ferreira, M.F. Montemor, W. K. Wijting, S. Toews, G. Grundmeier, The combined use of scanning vibrating

electrode technique and micro-potentiometry to assess the self-repair processes in defects on “smart” coatings applied to galvanized steel, Electrochim. Acta 56 (2011) 4475–4488, https://doi.org/10.1016/j.electacta.2011.02.048.
[36] M.G. Taryba, S.V. Lamaka, Plasticizer-free solid-contact pH-selective microelectrode for visualization of local corrosion, J. Electroanal. Chem. 725 (2014) 32–38, https://doi.org/10.1016/j.jelechem.2014.04.016.
[37] B.V.G. De Viveiros, U. Donatus, M.C. De Alencar, L.O. Berbel, I. Costa, Comparing the corrosion behaviour of AA2050 and AA7050 aluminium alloys by scanning vibrating electrode and scanning ion-selective electrode techniques, corrosion engineering, Sci. Technol. 57 (2021) 85–96, https://doi.org/10.1080/1478422X.2021.1992132.